PROCEEDINGS OF SPIE

SPIEDigitalLibrary.org/conference-proceedings-of-spie

Laser-induced forward transfer as a versatile tool for developing silicon-based anode materials

Rist, U., Reif, A., Pfleging, W.

U. Rist, A. Reif, W. Pfleging, "Laser-induced forward transfer as a versatile tool for developing silicon-based anode materials," Proc. SPIE 11989, Laser-based Micro- and Nanoprocessing XVI, 119890C (4 March 2022); doi: 10.1117/12.2609588

SPIE.

Event: SPIE LASE, 2022, San Francisco, California, United States

Laser-induced forward transfer as a versatile tool for developing silicon-based anode materials

U. Rist, A. Reif, W. Pfleging

Karlsruhe Institute of Technology, IAM-AWP, P.O. Box 3640, 76021 Karlsruhe, Germany

ABSTRACT

Further efforts are needed to increase the power and energy density of lithium-ion batteries. This increase can be achieved by developing new electrode architectures and new active materials. As a new active material for anodes, silicon is in the focus of current research, as it has an order of magnitude higher specific energy density compared to the commonly used graphite. In terms of new architecture, printing anodes with the "laser induced forward transfer" (LIFT) process offers a variety of possibilities. For this work, printing with LIFT adapted anode paste was realized and corresponding laser parameters were optimized. The anodes were printed with graphite for subsequent analyses in a coin cell and compared with state-of-the-art coated electrodes made with the same paste. The conventional coated electrodes were either calendered or uncalendered. It was shown that the electrochemical behavior of the printed anodes is comparable to that of the conventional coated anodes. Finally, preliminary studies were made to print an anode with a multilayer architecture. Within the anode layer, which consists of three individual printed layers, silicon layers are incorporated in order to significantly increase the specific capacity.

Keywords: LIFT, printing, anodes, lithium-ion battery, 3D battery

1. INTRODUCTION

Further efforts are needed to increase the electrochemical performance of lithium-ion-batteries to make electrical mobility more attractive. To achieve a boost in performance, new electrode architectures such as the 3D battery concept and new electrode materials must be introduced [1]. Silicon is in the focus of research as a new electrode material. Silicon has one order magnitude higher specific capacity (3579 mAh/g) [2] compared to natural graphite (372 mAh/g) [3]. However, silicon exhibits a volume expansion of 300 % during lithiation in comparison to 10 % of graphite during lithium intercalation. A large volume expansion leads to a tremendous mechanical degradation of the anode, resulting in a loss of capacity and a limited lifetime [4]. Printing of electrodes via LIFT offers new possibilities to develop advanced electrode

Laser-based Micro- and Nanoprocessing XVI, edited by Akira Watanabe, Rainer Kling, Proc. of SPIE Vol. 11989, 119890C · © 2022 SPIE
0277-786X · doi: 10.1117/12.2609588

architectures [5]. LIFT of micro batteries [6] and printed and subsequently structured cathodes [7] are already realized in research. In the current study, anodes are printed in a large format for testing in coin cells. These printed anodes are electrochemical cycled against lithium ("half-cells"). The characterization includes several cycles at different C-rates, ranging from C/10 up to 3C. The term "C-rate" describes the applied electrical current which is divided by the practical capacity of the battery. The printed electrodes are compared with conventional coated ones using the same paste ("slurry"). Furthermore, first results of a new anode architecture using graphite and silicon are presented. Hereby, the silicon is incorporated as a layer within a multilayered anode. However, the optimization of the slurry and the printing process is still under development and electrochemical data are currently under evaluation.

2. EXPERIMENTAL SET-UP

Figure 1 shows a schematic view of the LIFT process. In the current study, the applied laser (Lumentum, USA, Model: Q301-HD-1000R) has a maximum power of 10 W and a maximum repetition rate of 30 kHz. The operational wavelength is 355 nm. The pulse width is 78 ns. A DOE optic is applied to achieve a top-hat laser intensity profile. A mask selector provides different aperture shapes like squares and circles for subsequent printing. Via objective lens a demagnification of a selected aperture by a factor of 3.5 takes place.

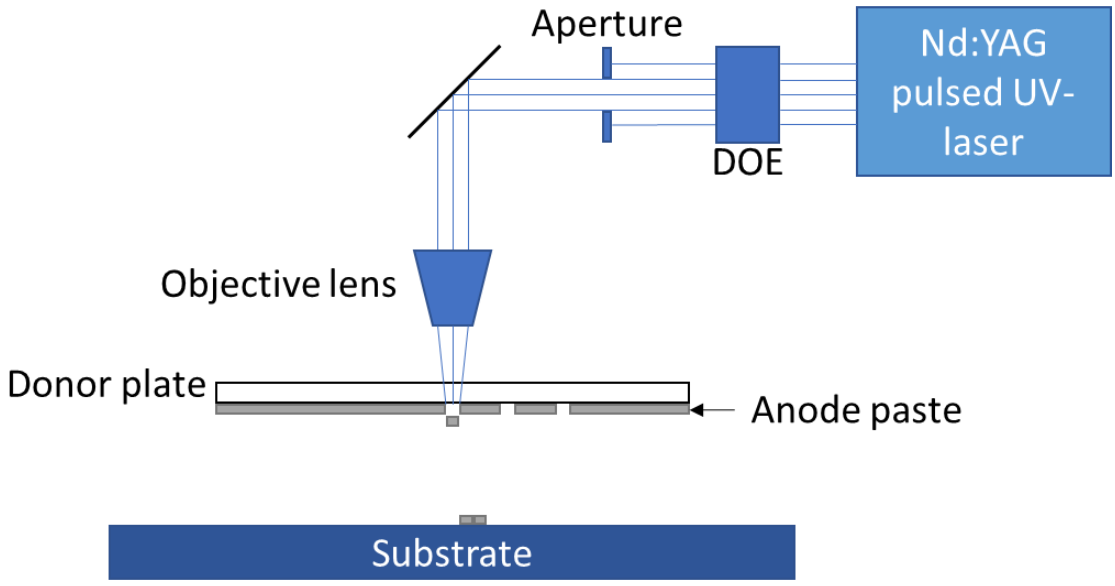

Figure 1: Schematic representation of the applied LIFT process.

The donor plate is a circle quartz glass wafer (DSP-200×0675-SGQ-00, Wafer Universe, Germany) with a diameter of 200 mm and a thickness of 0.675 mm. The paste used for printing electrodes for the coin cell analyses contains 85 wt.% mesocarbon microbeads (MCMB) synthetic graphite (PO0120, MSE Supplies, USA). The graphite particles have an average particle size of d_{50} = 12.2 µm, measured with laser scattering (LA-950, Horiba, Japan). In addition, the paste contains 5 wt.% carbon black (Super C65, Timcal, Swiss). The binder polyvinylidene fluoride (PVDF) (Solef 5130,

Solvay, Belgium) is added with an amount of 10 wt.% and the solvent is N-methyl-2-pyrrolidone (NMP) (806072, Merck, Germany). The viscosity of the slurry was measured with a parallel plate viscosimeter (MCR72, Anton Paar, Germany) and reaches a value of 16.5 Pa·s at a shear rate of 50 1/s. The paste used for the preliminary studies with silicon contains 40 % nanopowder silicon (SI-15008, Targray, Canada) with an average particle size of d_{50} = 72 nm. The slurry also contains 40 % carbon black and as binder 20 % of PVDF. The solvent is NMP and the viscosity, measured as mentioned above, is 1.29 Pa·s at a shear rate of 50 1/s.

For anode printing, the LIFT process of fluids is used, as described by Fernández-Pradas [8]. The slurry is deposited onto the donor plate via a doctor blade, which is set to a gap of 40 µm. During the LIFT process, the distance between the anode layer and the copper foil substrate is set to 180 µm. The spacing between the individual ablations on the donor plate is 0.25 mm. The laser repetition rate is 10.8 kHz. The used aperture generates a squared laser beam onto the donor plate with a side length of 83 µm. The laser fluence for the printing process takes 0.89 mJ/cm^2. For the coin cell design, areas of each 13x13 mm are printed. Subsequently, the printed electrode is cut into the desired shape with an ultrafast laser operating at a wavelength of 515 µm. The final anodes have a circular design with a diameter of 12 mm. The printed electrode is assembled in a coin cell for electrochemical analyses. Hereby, the coin cells are built as half-cells versus lithium as counter electrode. The circular lithium has a diameter of 15 mm and the applied polypropylene separator (EQ-bsf-0025-60C, Celgard, USA) has a diameter of 19 mm. The cells are analyzed with a BT 2000 (Arbin Instruments, USA) providing 32 channels and the software version MitsPro 4.0. The cells are cycled in a voltage window of 0.1 - 1.5 V. Charging consists of a constant current (CC) phase, whereas discharging additionally uses a constant voltage (CV) phase which corresponds to the lithiation of the printed electrode. For the formation of the printed electrode, cycling is performed three times at C/20 with a cut-off current of C/50 for the CV phase. The cells are subsequently cycled at different C-rates, from C/10 up to 3C, to investigate the charging and discharging behavior.

3. RESULTS & DISCUSSION

Voxel transfer

In addition to the distance between the donor plate and the substrate, the average laser power is also important for the transfer of a single voxel. In Figure 2 , the required laser fluence for LIFT is plotted as a function of the laser illuminated area (“laser spot size”) on the donor plate.

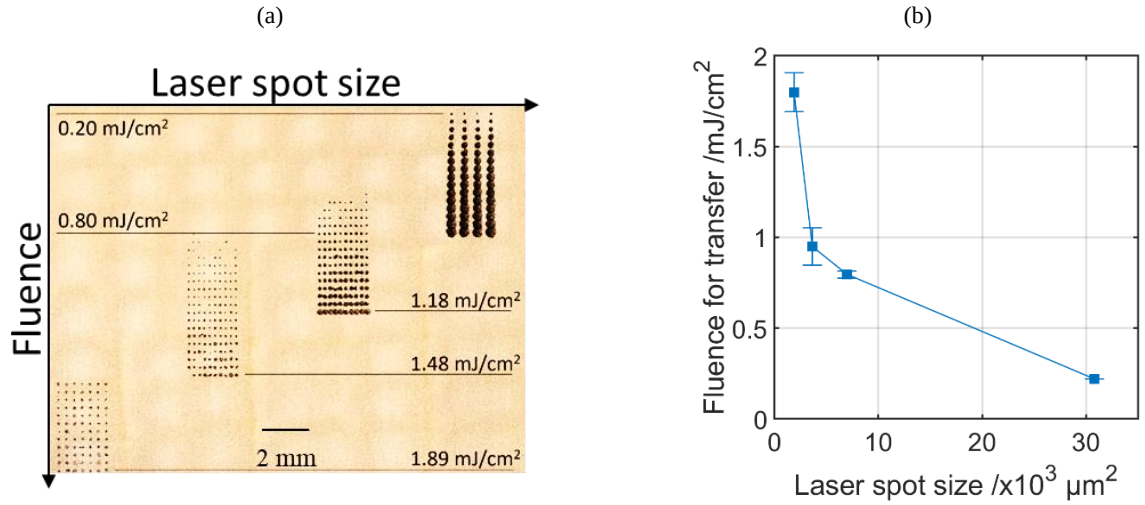

Figure 2: Laser fluence required for a single voxel transfer. (a) transferred voxels, the printing process started at a fluence 0.132 mJ/cm^2 for each column. (b) the required laser fluence as a function of laser illuminated area (laser spot size) on donor plate.

Figure 2a shows a microscopic image of transmitted voxels realized with four different aperture types leading to different laser spot sizes and so to different voxel sizes. Hereby, the voxels of the left column are printed with the smallest laser spot size, and the voxels on the right side are printed with the largest laser spot. The fluence was increased from top to bottom of the picture, for each column the printing process started at a fluence of 0.132 mJ/cm^2 with a step-wise increase of about 0.041 mJ/cm^2 per row. In Figure 2b, the fluence required for a transfer is as a function of laser spot size. It can be seen that the required laser fluence is low for large laser spot size and increases as the laser spot size becomes smaller. Thus, with a smaller laser spot size, a significantly higher energy density is required for the printing process. This is in accordance to the result of Fernández-Pradas et al. [9], which used a gaussian beam profile and different focusing conditions to vary the spot size.

Laser direct writing

For printing a single line, Serra et al. [10] have shown that a process adapted overlap of the individual voxels is necessary to obtain an accurate material transfer. With a water–glycerol solution, it needs to be an overlap of 50 % to obtain an accurate printed line. The laser illuminated squared area used for the transfer has a size of 83x83 µm. A point-to-point distance of 0.07 mm has proven to be optimal.

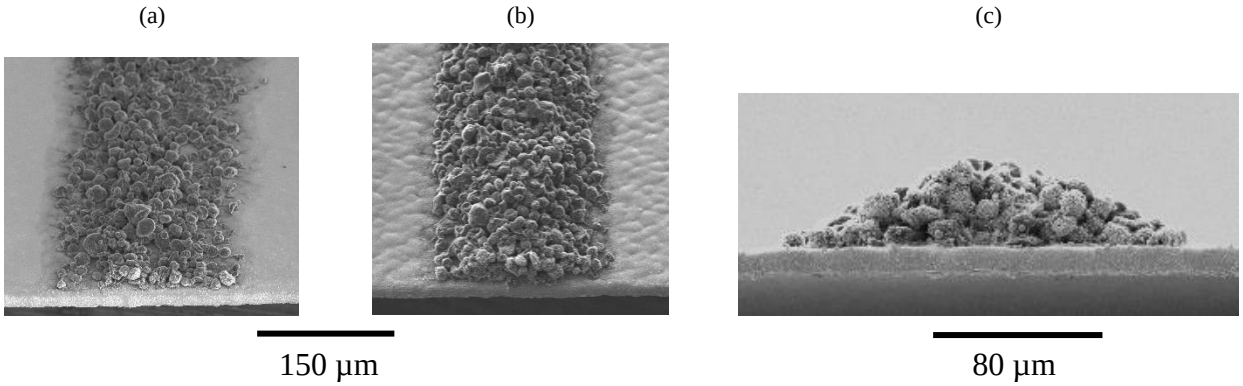

Figure 3: Scanning electron microscope (SEM) images of printed lines: (a) top view (one printing repetitions), (b) top view (five printing repetitions) and (c) cross-sectional view (five printing repetitions).

Figure 3a shows a printed track after one single LIFT cycle. After one printing cycle the layer thickness is in the range of the particle size and at some locations along the line the current collector is exposed. Therefore, for the printing of lines, it is very useful to print them with multiple reprints in order to obtain a high mass loading and a high coverage ratio of active material on the current collector surface. Figure 3b shows a top view of a printed line which is printed with five printing repetitions. The line has a high coverage ratio of active material on the current collector surface. Figure 3c shows the shape of the line in cross-section after five printing cycles. Hereby, a continuous active layer with a parabolic cross-sectional shape can be realized. The parabolic shape is explained by the slurry`s viscosity. According to Mathews et al. [11], a viscosity between 90 and 150 Pa·s is needed to print sharp-edged objects.

Areal material transfer

During areal printing, each voxel, with the exception of those at the edges, is overlaid by other voxels in the printing direction and perpendicular to it. Because of this and the low used viscosity, the accurate transfer of the individual voxels is not as critical as in the case of single voxel or line writing. For areal printing, the processing time has to be considered as a limiting factor. The laser fluence must be selected in a way that the material transfer can still be implemented until the end of the process.

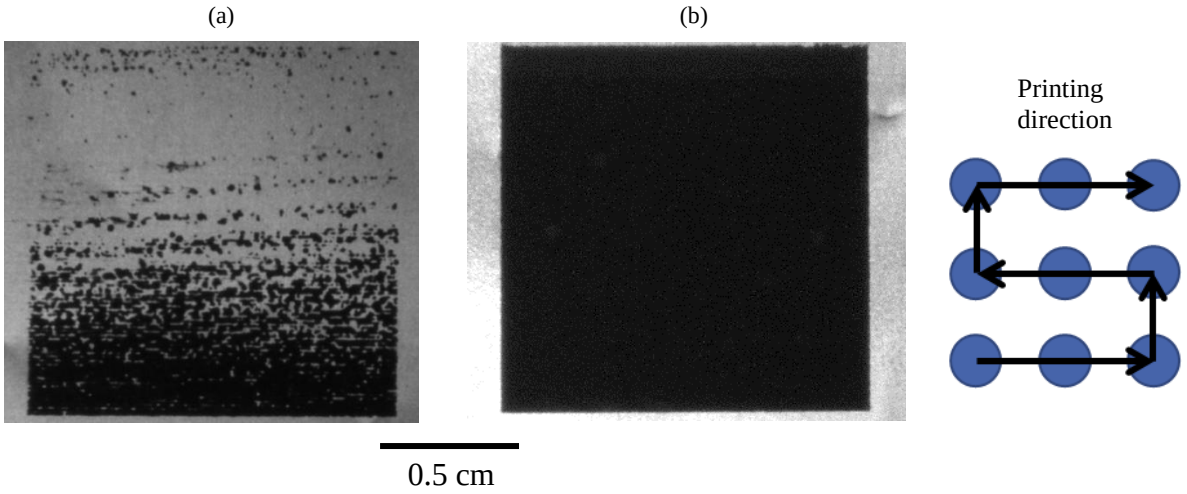

Figure 4: Areal print with a size of 13x13 mm: (a) microscopic image of an example with insufficient material transfer (0.55 mJ/cm^2), (b) material transfer with high homogeneity (0.76 mJ/cm^2).

Figure 4a shows a printed area after the first printing cycle. During the printing process, the material transfer occurs well at the beginning, but the slurry on the donor plate is slightly changing its viscosity as a function of time resulting in an insufficient material transfer during the process. Figure 4b shows that this bottleneck in printing can be overcome by the selection of a slightly higher energy density. It can be seen that one printing cycle is sufficient for achieving an areal print with homogenous mass distribution without macroscopic distortions. With the used process parameters - a voxel-to-voxel and line-to-line distance of 0.07 mm, a line length of 13 mm and a printing speed of 2.5 mm/s - the LIFT process takes more than 16 min for an areal print of 13x13 mm.

The layer thickness of the printed electrode can be adjusted using two different approaches. On the one hand, the layer thickness on the donor plate can be varied and, on the other hand, the same area can be printed with several printing cycles. When printing is repeated several times on the same surface, it is worth mentioning that between individual layers a 90° rotation of the print line hatching should be performed, otherwise a significant surface roughness of the printed layer will be achieved. Figure 5 shows cross-sections of printed surfaces for different numbers of printing cycles.

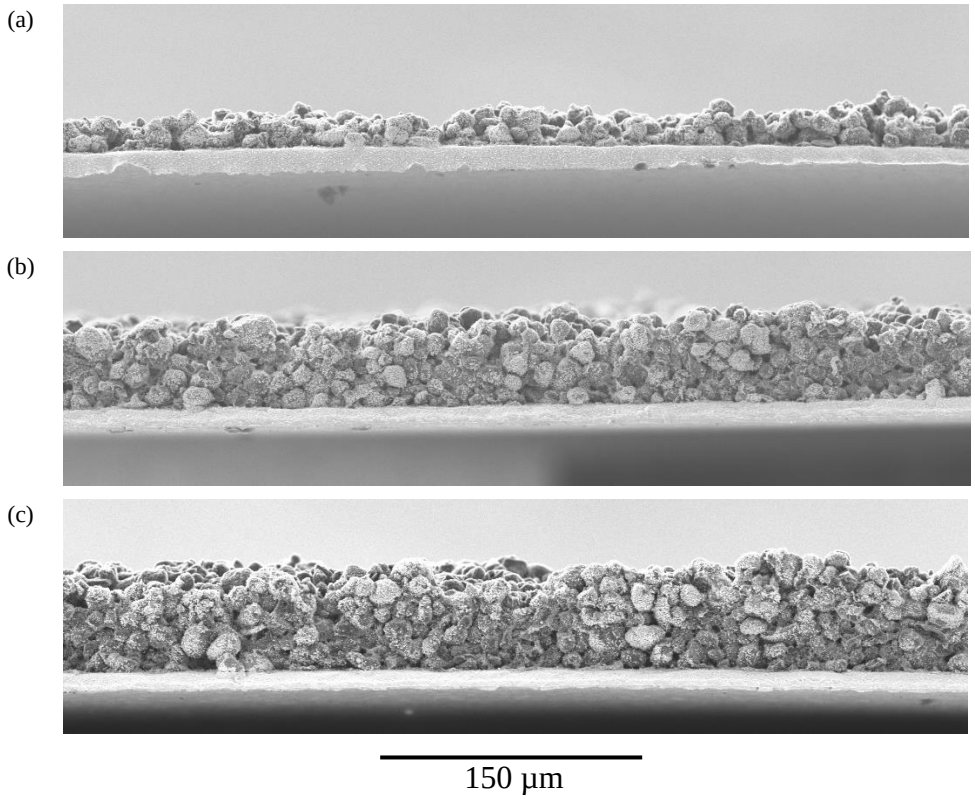

Figure 5: SEM of printed electrodes (cross sectional view) for different numbers of printing cycles: (a) one printing cycle (average layer thickness 20 µm), (b) three printing cycles (average layer thickness 50 µm), and (c) five printing cycles (average layer thickness: 58 µm).

Figure 5a shows a surface after one printing cycle. It can be seen that the surface roughness reflects the variation of individual particle sizes. After three cycles the layer has an average thickness of about 50 µm which would correspond to a film growth rate of about 16 µm per printing cycle. However, after five cycles the layer thickness is about 58 µm, i.e., the film growth rate becomes less than 12 µm per printing cycle. To achieve a more linear growth of layer thickness with number of printing cycles, further slurry and process optimization is required.

Electrochemical analysis

For electrochemical analysis graphite electrodes were printed using three printing cycles and subsequently assembled in coin cells versus lithium. For comparison, state-of-the-art electrodes are also fabricated by tape casting using the same slurry. Reference coin cells are assembled with either uncalendered or calendered electrodes. Uncalendered reference electrodes are taken into consideration due to the fact that the printed electrodes are also not calendered prior to cell assembly. The cells are cycled at different C-rates from C/10 up to 3C. In Figure 6 the specific discharge capacity is plotted against the C-rate, further information about the used electrodes is listed in Table 1.

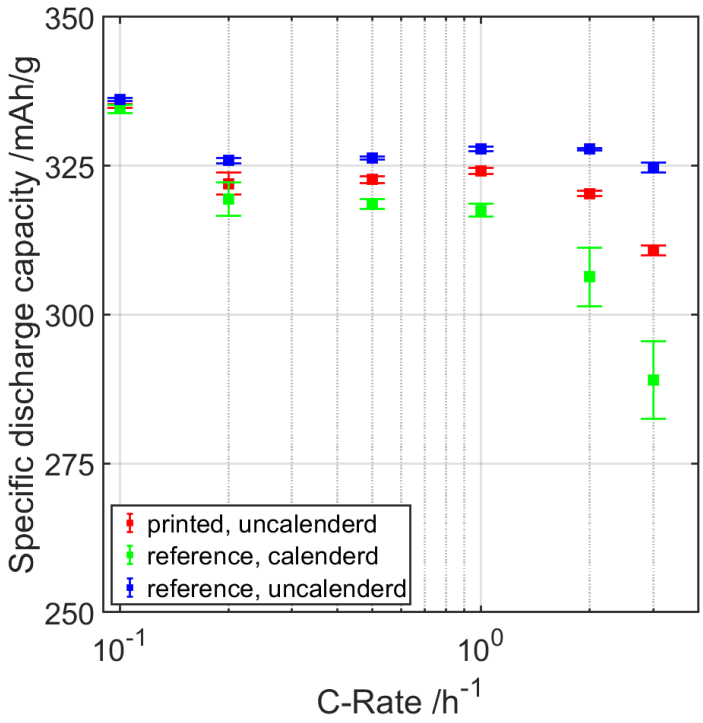

Figure 6: Specific discharge capacity as a function of C-rate for cells with printed uncalendered, coated calendered, and coated uncalendared electrode with similar specifications (see Table 1).

Figure 6 shows the specific discharge capacity of reference cells and cell with printed electrodes for C-rates from C/10 up to 3C. Below a C-rate of 2C, the specific discharge capacities of the cells are quite close to each other. Above a C-rate of 2C, a different behavior in capacity retention can be observed. The capacity values of the cell with printed electrode is lower compared to the cell with uncalendared electrode. This behavior might be due to the multilayer structure of the printed electrode which induces a slight variation in binder distribution at the layer interfaces. Also a slightly higher active mass loading is given for the printed electrode which would also counteract to the high power operation. The calendered cell shows a reduced capacity retention at higher C-rates due to the small porosity value. For C-rates up to 2C, the cell with uncalendered reference electrodes match well with the specific capacity data of the cell with the printed electrode. It is obvious that the active material of the electrode is not damaged or modified during the LIFT process and the electrochemical behavior of the cell with printed electrodes in terms of discharge ability is quite close to the cells with reference electrodes.

Table 1: Thickness, porosity, calculated specific area capacity, and mass loading of the active material of used electrodes.

Electrode type	Thickness	Porosity	Spec. capacity	Mass loading
-	µm	%	mAh/cm^2	mg/cm^2
printed, uncalendered	53	48.7	1.61	0.123
reference, calendered	44	40	1.55	0.122
reference, uncalendered	51	48.2	1.53	0.121

Table 1 shows the thickness, porosity, calculated specific area capacity, and mass loading of the used electrodes. The porosity of the printed electrodes and the reference uncalendered electrodes are in a similar range. The layer thickness of the calendered electrode was adjusted in order to reach a porosity of 40 % which is in good agreement with porosity values for conventional graphite electrodes [12].

Multilayer deposition

As a new electrode architecture, a multilayer is printed with one layer graphite on top of the current collector and subsequent two layers of silicon, see Figure 7.

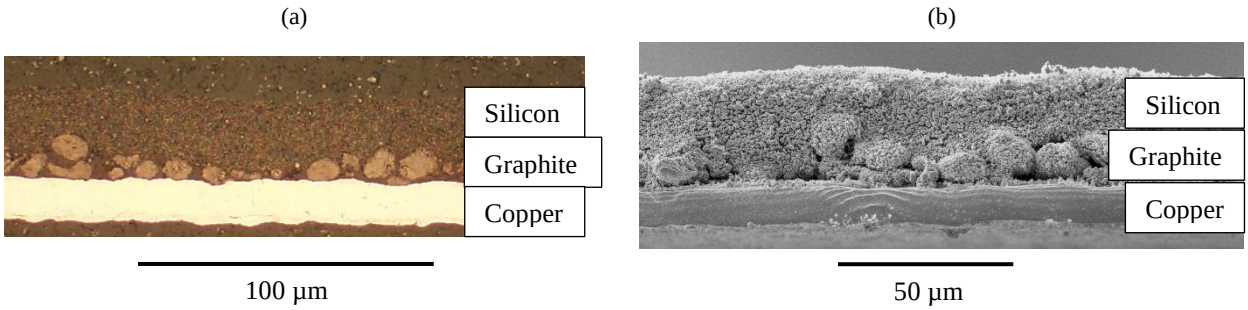

Figure 7: Cross-sectional view of printed multilayer electrode with one layer graphite and two layers of silicon, (a) microscope image of printed electrode, (b) respective SEM image.

Figure 7 shows cross-sectional views of a printed multilayer electrode, a light microscope image of an embedded multilayer (Figure 7a) and a SEM image (Figure 7b). A porous and thin graphite particle layer and a dense layer of silicon nanoparticles can be recognized. It can be seen that the final printed surface has a compact structure and a slight waviness. The solid content of the silicon slurry is significantly lower than that of the graphite one. The printing and subsequent drying of the silicon layer is therefore more sophisticated than that of the graphite. The silicon slurry optimization and the assembling of the new printed electrode architecture in coin cells is ongoing.

4. CONCLUSION & OUTLOOK

LIFT for manufacturing graphite anodes and the subsequent construction of batteries in coin cell format was realized. During LIFT, the required laser energy density is a critical parameter and needs to be adjusted as a function of voxel size and processing time. The process duration must be taken into account due to the impact of time-dependent slurry viscosity on printing quality. The average laser power must therefore be chosen appropriately at the beginning of the process. The printed electrodes show a similar porosity as the uncalendered electrodes, so uncalendered layers were also analyzed as reference. The electrochemical analysis shows that the printed electrodes have a similar discharge behavior as the reference electrodes, calendered or uncalendered ones. This leads to the conclusion that the active material is not modified during the LIFT process. Finally, electrodes with a multilayer architecture can be synthesized via printing providing new opportunities in designing advanced electrode architectures, e.g., the incorporation of silicon layers into a graphite multilayer system.

Further efforts are needed to develop multilayer anodes for next-generation batteries. Different materials will be used for the individual layers to optimize their overall electrochemical and mechanical properties. Materials such as silicon will play a major role but different graphite types will also be considered. In addition to the anode materials, different binder-solvent systems will be taken into account. Furthermore, the areal printing concept will be expanded with regard to a 3D battery concept with embedded structures to improve the fast-charging and discharging capability. Further process optimization will also be required for the printing process itself with regard to slurry composition, thickness, and viscosity.

REFERENCES

[1] A. Meyer, F. Ball und W. Pfleging, *Nanomaterials (Basel, Switzerland)* **2021**, *11*, *DOI:* 10.3390/nano11123448.

[2] A. Baasner, F. Reuter, M. Seidel, A. Krause, E. Pflug, P. Härtel, S. Dörfler, T. Abendroth, H. Althues und S. Kaskel, *J. Electrochem. Soc.* **2020**, *167*, 20516, DOI: 10.1149/1945-7111/ab68d7.

[3] R. Korthauer, *Handbuch Lithium-Ionen-Batterien*, Springer Berlin Heidelberg, Berlin, Heidelberg, **2013**.

[4] W. Pfleging, *Nanophotonics* **2018**, *7*, 549–573, DOI: 10.1515/nanoph-2017-0044.

[5] D. Moldovan, J. Choi, Y. Choo, W.-S. Kim und Y. Hwa, *Nano convergence* **2021**, *8*, 23, DOI: 10.1186/s40580-021-00271-w.

[6] H. Kim, T. E. Sutto, J. Proell, R. Kohler, W. Pfleging und A. Piqué, in: *Laser-based Micro- and Nanoprocessing VIII* (Hrsg.: U. Klotzbach, K. Washio and C. B. Arnold), SPIE, **2014,** 89680L.

[7] P. Smyrek, H. Kim, Y. Zheng, H. J. Seifert, A. Piqué und W. Pfleging, in: *Laser 3D Manufacturing III* (Hrsg.: B. Gu, H. Helvajian and A. Piqué), SPIE, **2016,** 973806.

[8] Juan M. Fernández-Pradas, in: *Laser Printing of Functional Materials* (Hrsg.: A. Piqué and P. Serra), John Wiley & Sons Incorporated, Newark, **2017**.

[9] M. Colina, M. Duocastella, J. M. Fernández-Pradas, P. Serra und J. L. Morenza, *Journal of Applied Physics* **2006**, *99*, 84909, DOI: 10.1063/1.2191569.

[10] A. Palla-Papavlu, C. Córdoba, A. Patrascioiu, J. M. Fernández-Pradas, J. L. Morenza und P. Serra, *Appl. Phys. A* **2013**, *110*, 751–755, DOI: 10.1007/s00339-012-7279-6.

[11] S. A. Mathews, R. C. Y. Auyeung, H. Kim, N. A. Charipar und A. Piqué, *Journal of Applied Physics* **2013**, *114*, 64910, DOI: 10.1063/1.4817494.

[12] J. B. Habedank, F. J. Günter, N. Billot, R. Gilles, T. Neuwirth, G. Reinhart und M. F. Zaeh, *Int J Adv Manuf Technol* **2019**, *102*, 2769–2778, DOI: 10.1007/s00170-019-03347-4.